applied sciences

MDPI

Article

In Situ Stress Inversion in a Pumped-Storage Power Station Based on the PSO-SVR Algorithm

Lu Liu [1,*], Jinhui Ouyang [1,2,*], Genqian Nian [3], Youping Zhu [1,2] and Ning Liang [3]

[1] China Three Gorges Corporation, Wuhan 430010, China; zhu_youping@ctg.com.cn
[2] China Three Gorges Corporation Science and Technology Research Institute, Beijing 101100, China
[3] Institute of Geophysics and Geology, Chinese Academy of Sciences, Beijing 100029, China; nian_gengqian@ctg.com.cn (G.N.); liangning@mail.iggcas.ac.cn (N.L.)
* Correspondence: liu_lu8@ctg.com.cn (L.L.); ouyang_jinhui@ctg.com.cn (J.O.)

Abstract

An accurate in situ stress field is a prerequisite for evaluating the stability of surrounding rock in underground caverns of a pumped-storage power station (PSPS) and ensuring the long-term safe operation of underground powerhouses. However, in situ stress measurements in the field are typically characterized by a limited number of measurement points, strong data randomness, and high testing costs. Meanwhile, conventional regression inversion methods often yield stress fields with insufficient accuracy or unstable spatial distributions. To address these issues, this paper proposes an in situ stress field inversion method based on the particle swarm optimization–support vector regression (PSO-SVR) algorithm. Stress boundary conditions are formulated in terms of lateral stress coefficients combined with shear stresses, and PSO is employed to optimize the hyperparameters of the SVR model. The stress boundary conditions predicted by the PSO-SVR algorithm are then imposed on a numerical model to compute the stresses at the measurement points, and the optimal boundary conditions are identified by minimizing the root mean square error (RMSE) between the inverted and measured in situ stresses. On this basis, the stress components at the measurement points and the in situ stress field in the study area are obtained. The results demonstrate that the inverted in situ stresses agree well with the field measurements, exhibiting good consistency and spatial regularity. Specifically, compared with the traditional multiple linear regression (MLR) method, the PSO-SVR algorithm reduces the RMSE and mean absolute error (MAE) of the in situ stress measurement data by 48.21% and 47.01%, respectively, and produces inversion results with higher accuracy, more stable spatial patterns, and markedly fewer anomalous zones. Consequently, the PSO-SVR algorithm is well suited for in situ stress inversion in PSPSs and provides a reliable stress-field basis for subsequent optimization of underground cavern excavation and support.

Keywords: pumped-storage power station; in situ stress inversion; lateral stress coefficient; particle swarm optimization (PSO); support vector regression (SVR); multiple linear regression (MLR); finite-difference modelling

Check for updates

Academic Editor: Tiago Filipe da Silva Miranda

Received: 10 December 2025
Revised: 17 January 2026
Accepted: 18 January 2026
Published: 21 January 2026

Copyright: © 2026 by the authors. Licensee MDPI, Basel, Switzerland. This article is an open access article distributed under the terms and conditions of the Creative Commons Attribution (CC BY) license.

1. Introduction

In situ stress refers to the natural stress state of a rock mass prior to disturbance by engineering activities [1,2]. For underground caverns of a pumped-storage power station (PSPS), reliable information on the orientation, magnitude, and spatial distribution of the

in situ stress field is fundamental for assessing surrounding-rock stability and ensuring the long-term safe operation of the underground powerhouse [3,4]. For example, the axis of the underground main powerhouse is commonly arranged to form a small angle with the maximum principal stress direction as to mitigate the adverse effects of in situ stress on surrounding-rock stability. Field measurements provide the most direct means of characterizing the in situ stress state. In practice, the number of measurement points is generally limited by site conditions, costs, and time constraints. Moreover, the in situ stress field is jointly controlled by multiple geological and topographic factors and is also affected by measurement uncertainty, which means that the measured stresses often exhibit considerable scatter [5]. Consequently, numerical inversion methods that integrate limited in situ stress measurements with engineering–geological information have become practical and widely used tools in underground engineering. These methods enable extrapolation from sparse measurements to an in situ stress field [6].

Regression inversion is one of the most commonly used numerical methods for reconstructing in situ stress fields, in which stress boundary conditions are evaluated by comparing numerically computed stresses against in situ measurements. Within this framework, multiple linear regression (MLR) has been the most widely used method. By regressing the measured in situ stresses against the numerically computed results and solving for the regression coefficients, the boundary-condition combination that best fits the measurements can be inferred. The corresponding in situ stress field is then reconstructed [7,8]. For example, Li et al. [9] proposed a modified MLR method for in situ stress that combines partial least-squares with zonal loading and thereby improved the accuracy of the in situ stress field at the Dagangshan hydropower station. Chen et al. [10] employed the MLR method to invert the in situ stress field of a deeply buried tunnel in a high-geothermal environment. Zhou et al. [11] proposed a new MLR method with unified displacement boundary conditions to improve the accuracy of in situ stress for a tunnel. However, MLR typically assumes that the boundary-condition parameters are mutually independent and linearly related to the response. In combination with the usually limited number of measurement points, this can lead to results that reproduce the measured stresses reasonably well at the measurement locations but exhibit abrupt variations or spurious anomalies in the stress field.

To overcome these limitations, a variety of data-driven methods based on machine learning or artificial intelligence have been introduced into in situ stress inversion. For example, Li et al. [12] proposed a neural-network model for inversion of in situ stress in the Xiluodu area. Song et al. [13] developed an LSTM-hybrid optimization (LSTM-HO) model for nonlinear inversion of in situ stress fields in stratified rock masses with deep valleys, helping to alleviate the non-uniqueness of model boundary conditions. Li [14] employed a support vector machine (SVM) model to invert the in situ stress field of deep mine roadways from measured horizontal stress and pore-pressure data. The inverted results agreed well with the field data. In addition, hybrid algorithms such as gradient descent–particle swarm optimization (GD-PSO) [15], genetic-algorithm–optimized generalized regression neural networks (GA-GRNN) [16], and stepwise-regression–differential-evolution–support-vector machine (SR-DE-SVM) [4] have been employed for in situ stress inversion analysis, achieving good results. However, these inversion algorithms share a common drawback. During model training, displacement or stress boundary conditions are typically treated as output variables, while stress values are used as input variables. Once an "optimal" set of boundary conditions is obtained, it is then directly imposed on the physical boundaries of the numerical model. Under such a procedure, during the iterative equilibrium process, especially near model boundaries or in regions with pronounced topographic variations, significant differences in the prescribed displacement rates or stress values at adjacent

elements or nodes can give rise to local zones of abrupt stress change. This, in turn, may degrade the overall accuracy and smoothness of the reconstructed in situ stress field in the study area.

Compared with conventional hydropower projects, PSPSs are often characterized by relatively limited geological investigation and sparse in situ stress measurements at the preliminary stage. In addition, in situ stress is generally determined by hydraulic fracturing. As a result, the available datasets are typically high-dimensional, nonlinear, and strongly stochastic, reflecting both the testing principle and various field constraints. To cope with such data characteristics, SVR is well suited to small-sample, high-dimensional, and nonlinear problems, and offers good generalization capability and robustness while maintaining a reasonable level of computational efficiency. When combined with particle swarm optimization (PSO) for hyperparameter tuning, the resulting PSO-SVR algorithm can further enhance the efficiency of parameter search and the overall fitting accuracy. In this context, a PSPS was adopted as the case study. A three-dimensional mesh model that incorporates the engineering–geological information is constructed, and stress boundary conditions are specified in terms of lateral stress coefficients combined with shear stress components on the model boundaries. Using a three-dimensional finite-difference code, in situ stress components at the measurement points are computed under a series of boundary-condition scenarios, thereby generating a "boundary-condition-stress" dataset. Those datasets are then used to train a PSO-SVR algorithm, which simultaneously determines the optimal hyperparameters and learns the nonlinear mapping between boundary conditions and stresses. The measured in situ stresses are subsequently input into the trained algorithm to infer the optimal boundary conditions, which are reimposed on the numerical model to reconstruct the in situ stress field throughout the study area. Finally, MLR is adopted as a baseline method for comparison, so as to quantify the improvement of PSO-SVR in in situ stress inversion.

2. Engineering Geological Conditions of the Project Area

The project area is located in the Qinglongshan mountainous region and is characterized by medium–low mountain terrain. The regional topography generally descends from southeast to northwest, with a maximum elevation of 2094.30 m. The underground powerhouse cavern group lies at a depth of approximately 455–495 m below the surface. The overlying strata belong to the Cambrian Zhangxia, Mantou, and Zhushadong formations. The stratigraphy can be simplified into four nearly parallel layers (Figure 1), with an overall attitude of 290°/NE∠38°. From top to bottom, the lithologies are limestone, argillaceous siltstone, dolomite, and quartz sandstone, with approximate thicknesses of 340 m, 36 m, 43 m, and 407 m, respectively. Two dominant joint sets are identified, with orientations of 290–300°/NE∠80–85° and 280–290°/NW∠65–75°, respectively. Two major fault fracture zones, F10 and F11, exert significant influence on the area; their actual thicknesses are approximately 1.0 m and 1.5 m, and their strikes range from N 45° W to N 70° W. The groundwater table along the water conveyance–power generation system is relatively deep, with a typical burial depth of approximately 250–480 m. Groundwater activity is generally limited, and the rock mass shows poor water-bearing capacity. Moreover, the limestone, dolomite, and quartzite strata are weakly permeable, whereas the argillaceous siltstone stratum is relatively less permeable.

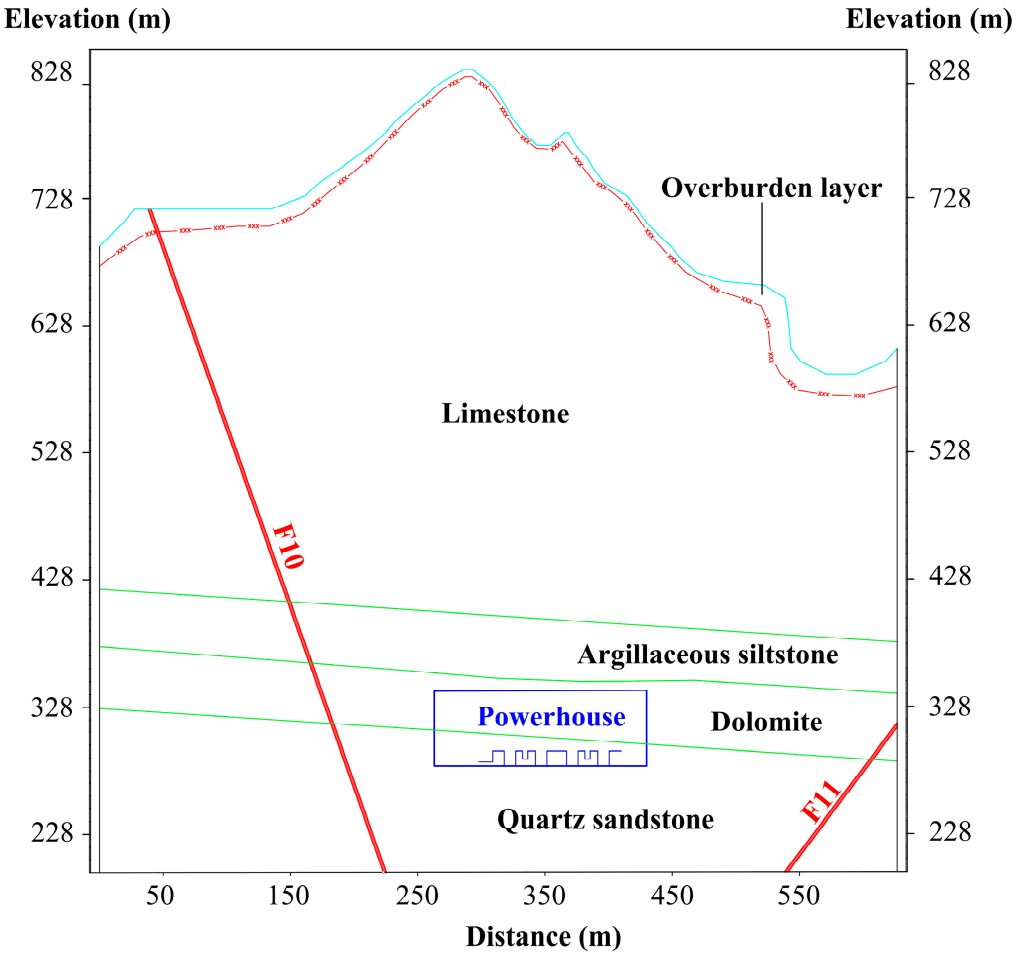


Figure 1. Engineering geological cross-section at x = 215 m.

Hydraulic fracturing tests for in situ stress determination are conducted in three boreholes (YZK06, YZK17, and YZK19), and the stress data are summarized in Table 1. At six measurement points, the three principal stresses satisfy $\sigma_H > \sigma_v > \sigma_h$, where σ_H is the maximum horizontal stress, σ_v is the vertical stress, and σ_h is the minimum horizontal stress, indicating that the in situ stress field in the project area is dominated by horizontal tectonic stresses. The azimuths of the hydraulic-fracturing-induced fractures range from 249° to 263°, implying that the maximum principal stress is oriented towards the west–southwest (WSW). In addition, all three principal stress components exhibit a clear increasing trend with burial depth, as shown in Figure 2.

Table 1. Results of in situ stress measurements by hydraulic fracturing in boreholes (σ_H-maximum horizontal stress; σ_v-vertical stress; σ_h-minimum horizontal stress).

Borehole ID	Buried Depth (m)	The Values of Principal Stresses (MPa)			Fracture Azimuth (°)
		σ_H	σ_v	σ_h	
YZK06	191.99	5.87	3.35	5.24	251
	300.09	9.57	5.24	8.18	251
YZK17	486.29	13.85	8.38	12.15	249
	554.29	15.80	9.01	13.86	249
YZK19	493.90	15.16	9.51	12.85	263
	533.90	14.40	9.00	13.85	263

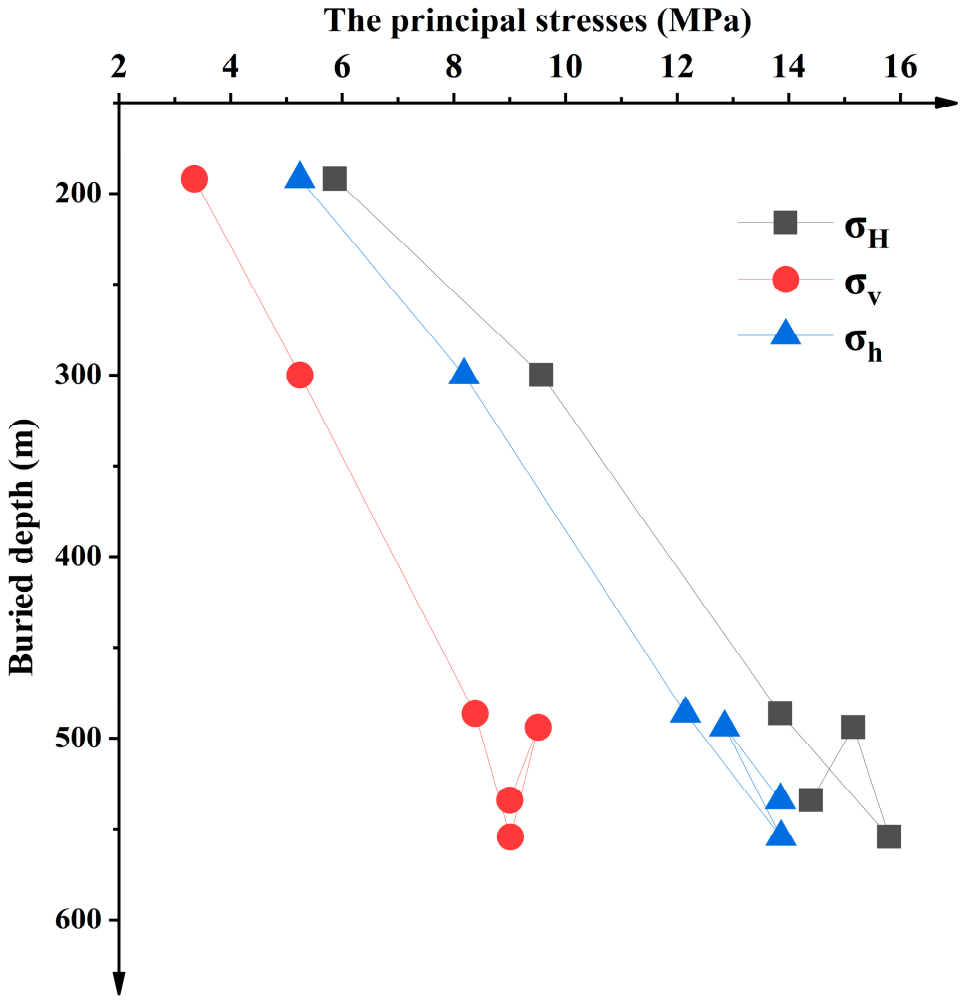


Figure 2. The relationship between principal stresses and buried depth.

3. In Situ Stress Inversion Using MLR

3.1. Basic Principles

The MLR inversion method is based on the principle of elasticity superposition. Under natural in situ stress conditions, the rock mass is assumed to be in mechanical equilibrium without continuous accumulation of plastic deformation. Accordingly, the complex in situ stress state acting on the rock mass can be decomposed into six basic boundary stress components, as shown in Figure 3: (1) tectonic compressive stress in the x direction; (2) tectonic compressive stress in the y direction; (3) gravitational stress; (4) xy shear stress; (5) xz shear stress; and (6) yz shear stress. For each basic component, a numerical model with unit boundary stress is constructed, and the corresponding stress components at the measurement points are obtained by numerical simulation. The numerically computed stress components are then used as independent variables and the measured in situ stresses as dependent variables in a least-squares multiple linear regression analysis to determine the regression coefficients. The regression equation can be expressed in the following general form [9]:

$$\hat{\sigma}_m = \sum_{i=1}^{n} L_i \sigma_m^i \quad (1)$$

where m is the index of the in situ stress measurement point; $\hat{\sigma}_m$ is the regressed value of the in situ stress at point m; σ_m^i is the stress component at point m obtained from numerical simulation; L_i is the MLR coefficient; n is the number of components, which is generally taken as six.

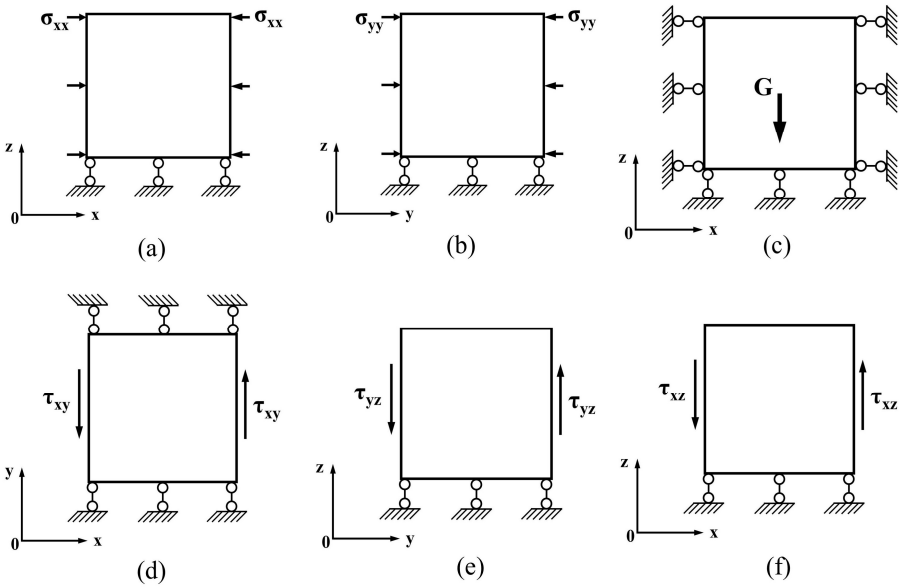


Figure 3. Six different boundary-condition components corresponding to the in situ stress ((**a**) tectonic compressive stress in the x direction; (**b**) tectonic compressive stress in the y direction; (**c**) gravitational stress; (**d**) xy shear stress; (**e**) xz shear stress; (**f**) yz shear stress).

If there are k in situ stress measurement points, the least-squares sum of squared residuals S_c can be written as

$$S_c = \sum_{m=1}^{k} \sum_{j=1}^{6} \left(\sigma_{jm}^{*} - \sum_{i=1}^{n} L_i \sigma_{jm}^{i} \right)^2 \quad (2)$$

where σ_{jm}^{*} is the measured stress component at point m.

According to the least-squares principle, setting the partial derivative of S_c with respect to each regression coefficient L_i to zero yields the following system of normal equations:

$$\frac{\partial S_c}{\partial L_i} = 0, i = 1, 2, \ldots, n \quad (3)$$

Solving Equation (3) provides the n regression coefficients:

$$L = (L1, L2, \ldots, Ln)^T \quad (4)$$

The in situ stress at any point Q within the study area can then be obtained by superposing the numerically computed stresses corresponding to the different loading cases:

$$\sigma_{jq} = \sum_{i=1}^{n} L_i \sigma_{jq}^{i} \quad (5)$$

where the subscript j denotes the six components of the initial in situ stress.

3.2. Three-Dimensional Geological Model and Rock Mass Mechanical Parameters

The three-dimensional mesh model is established in a Cartesian coordinate system in which the axis of the main powerhouse is taken as the y-axis, oriented approximately N83°E, with y ranging from 0 to 570 m. Using the left and right sidewalls of the powerhouse as lateral reference planes, the model is extended by 200 m on both sides, giving an x-range of 0–529.6 m. In the longitudinal direction, the upstream sidewall of the powerhouse is taken as the upstream reference plane and the model is extended 200 m upstream, whereas the downstream boundary is defined by the downstream sidewall of the tailgate chamber with an additional 200 m extension downstream. Vertically, the z-axis extends

from the ground surface down to an elevation of 0 m. The mesh model is generated using the Griddle plug-in developed by Itasca. The model contains 456,608 gridpoints and 592,711 zones, predominantly hexahedral in shape, as illustrated in Figure 4.

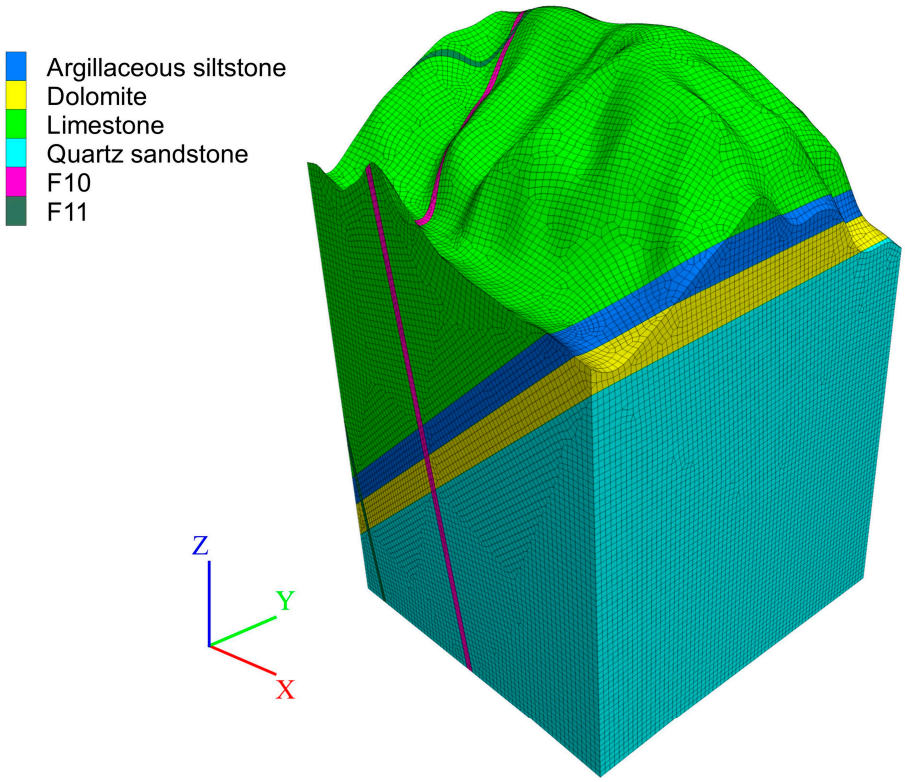


Figure 4. Three-dimensional geological numerical mesh model.

In the 3D mesh model, the faults are treated using a parameter-reduction (weakened-zone) approach: a fault influence zone extending 3–5 times the fault-zone width is defined on both sides of the fault, and reduced mechanical properties are assigned to both the fault core and the influence zone in the numerical calculations. All formations and fault zones are modeled using the Mohr–Coulomb constitutive model, and the corresponding parameters are listed in Table 2.

Table 2. Mechanical parameters of the rock masses.

Layer ID	Lithology	Density (g·cm^{-3})	Elastic Modulus (GPa)	Poisson's Ratio	Cohesion (MPa)	Friction Angle
Layer 1	Limestone	2.60	6.0	0.26	0.85	41.66°
Layer 2	Argillaceous siltstone	2.55	5.0	0.26	0.60	28.81°
Layer 3	Dolomite	2.65	6.0	0.26	1.00	43.53°
Layer 4	Quartz sandstone	2.70	10.0	0.24	1.10	45.00°
Fault (F10, F11)		2.15	1.00	0.30	0.45	4.57°

3.3. Results of In Situ Stress Inversion

Because the data are obtained from hydraulic fracturing tests, in which the vertical stress at the measurement points is assumed to coincide with one of the principal stresses, coordinate transformation yields zero xz and yz shear stresses at the measurement points. Accordingly, among the six boundary-condition components defined in Figure 3, only four

are retained: tectonic compressive stress in the x direction, tectonic compressive stress in the y direction, gravitational stress, and xy shear stress.

Because an elastic–plastic constitutive model is adopted in this study, whereas the MLR analysis is fundamentally based on the elastic linear superposition principle, an excessively large loading velocity (i.e., an overly large loading increment under a fixed number of steps) under displacement boundary conditions may cause local zones to yield prematurely. This leads to a pronounced nonlinearity in the stress–boundary–parameter relationship, thereby violating the superposition assumption and undermining the applicability and stability of the MLR. To address this issue, different boundary velocities are first applied in the X-normal direction with the same 2000 steps, and the resulting σ_{xx} values at the six monitoring points are compared, as summarized in Table 3. As shown in Table 3, when the velocity increases from 1×10^{-5} m/s to 5×10^{-5} m/s, σ_{xx} increases by approximately a factor of five. However, when the velocity further increases to 1×10^{-4} m/s, σ_{xx} at the six points becomes about 6.5–8.8 times that at 1×10^{-5} m/s, which deviates noticeably from the expected linear scaling corresponding to a tenfold increase in velocity. Similar trends are also observed at 5×10^{-4} m/s. Based on these results, a boundary loading velocity of 5×10^{-5} m/s is adopted in this study.

Table 3. σ_{xx} values at six monitoring points under different prescribed velocities in the X-normal direction.

ID	σ_{xx} (MPa)			
	10^{-5} m·s^{-1}	5×10^{-5} m·s^{-1}	10^{-4} m·s^{-1}	5×10^{-4} m·s^{-1}
YZK06(1)	−0.15	−0.75	−1.32	−2.91
YZK06(2)	−0.20	−1.00	−1.60	−4.04
YZK17(1)	−0.26	−1.28	−1.99	−5.36
YZK17(2)	−0.28	−1.39	−2.48	−10.01
YZK19(1)	−0.26	−1.30	−1.69	−2.73
YZK19(2)	−0.29	−1.47	−2.58	−10.21

In this paper, the in situ stress inversion is carried out using the zone-stress loading method proposed by Li et al. [9], and the procedure is implemented in the following steps:

Step 1: Fix the four faces of the numerical model at x = 0, y = 0, y = 570 m, and z = 0, and apply a boundary-normal velocity of 5×10^{-5} m/s to the x = 529.6 m face to compress the model in the x direction [9,17]. Run 2000 calculation steps, then record the six stress components at each measurement point and export the stress components for all zones.

Step 2: Remove all boundary conditions applied in Step 1. Then, in turn, apply the remaining three basic boundary conditions corresponding to tectonic compressive stress in the y direction, gravitational stress, and xy shear stress, as follows:

1. For tectonic compressive stress in the y direction, fix the four faces of the numerical model at x = 0, x = 529.6 m, y = 0, and z = 0, and apply a boundary-normal velocity of 5×10^{-5} m/s to the y = 570 m face to compress the model in the y direction;
2. For gravitational stress, fix the four lateral faces and the bottom face (x = 0, x = 529.6 m, y = 0, y = 570 m, and z = 0), and activate the gravitational body force in the model;
3. For xy shear stress, fix the four faces of the numerical model at x = 0, y = 0, y = 570 m, and z = 0, and apply a tangential velocity of 5×10^{-5} m/s in the y direction to the x = 529.6 m face to generate shear deformation in the xy plane.

For each loading case, run 2000 calculation steps, then record the six stress components at each measurement point and export the stress components for all zones.

Step 3: Use the stress components at the measurement points obtained under the four boundary conditions as independent variables and the measured in situ stress components as

dependent variables to construct an MLR model. Solve the model using the least-squares method to obtain the regression coefficients associated with the four boundary-condition components.

Step 4: Assign the in situ stress components for each zone, obtained from the MLR equations, to the numerical model. Run one calculation step to obtain the unbalanced nodal forces at all nodes. For each node, define an initial external nodal force that is equal in magnitude and opposite in direction to the corresponding unbalanced nodal force.

Step 5: Fix the four lateral faces and the bottom face of the numerical model (x = 0, x = 529.6 m, y = 0, y = 570 m, and z = 0). Reassign the in situ stress components to each zone and apply the initial nodal forces defined in Step 4. Then run the calculation until the model reaches equilibrium. The resulting stress state is taken as the reconstructed initial in situ stress field in the study area.

Using the above procedure, the regression coefficients corresponding to the four boundary conditions in the study area are obtained as $L_1 = 3.049$, $L_2 = 8.069$, $L_3 = 1.120$, and $L_4 = -39.642$, with a coefficient of determination of $R^2 = 0.894$. The stress components at the six measurement points calculated from the MLR equation are listed in Table 4. Overall, the normal-stress components show reasonable agreement with the measured values: apart from a few data points with noticeable deviations, such as σ_{yy} and σ_{zz} at YZK19(2) point, the mean deviation ratio (MDR) of the normal-stress components relative to the measurements is 17.16%. In contrast, the MDR of the τ_{xy} component reaches 100.87%, which is considerably higher than that of the normal stresses, indicating that the MLR inversion reproduces the shear stress much less accurately. This behavior mainly reflects two factors: τ_{xy} is not measured directly but inferred from hydraulic fracturing data under the assumption that one principal stress is vertical, so deviations from this assumption are amplified in the transformed shear component; moreover, within the MLR framework, τ_{xy} is governed essentially by a single boundary shear parameter, whereas the normal stresses are constrained by several boundary terms, so the limited number of measurement points provides much weaker regression constraints on τ_{xy} and leads to larger relative errors.

Table 4. Results of multiple linear regression analysis (IV: inverted values by MLR method; MV: measured values).

ID	σ_{xx} (MPa)		σ_{yy} (MPa)		σ_{zz} (MPa)		τ_{xy} (MPa)		τ_{yz} (MPa)		τ_{xz} (MPa)	
	IV	MV	IV	MV	IV	MV	IV	MV	IV	MV	IV	MV
YZK06(1)	−5.0	−3.8	−7.6	−5.4	−4.3	−5.2	−0.1	1.0	−0.4	0.0	1.0	0.0
YZK06(2)	−7.1	−6.1	−10.5	−8.7	−7.0	−8.2	−0.1	1.7	−0.2	0.0	1.1	0.0
YZK17(1)	−9.8	−9.6	−13.2	−12.7	−13.1	−12.2	0.3	2.3	0.3	0.0	0.6	0.0
YZK17(2)	−11.2	−10.5	−14.3	−14.3	−15.7	−13.9	0.1	2.8	0.5	0.0	1.3	0.0
YZK19(1)	−10.1	−9.8	−12.3	−14.8	−13.2	−12.9	0.3	1.3	0.4	0.0	1.2	0.0
YZK19(2)	−11.0	−9.3	−8.2	−14.1	−6.9	−13.9	−0.5	1.3	0.1	0.0	−0.5	0.0
Regression coefficients	$L_1 = 3.049$; $L_2 = 8.069$; $L_3 = 1.120$; $L_4 = -39.642$ c = 0.11(intercept of the regression equation)											
Coefficient of determination	$R^2 = 0.894$											

Figure 5 presents contour plots of the three normal-stress components along the axis of the main powerhouse (x = 215 m). Overall, the three normal stresses generally increase with depth below the ground surface, and this behavior is broadly consistent with the depth-dependent trend observed in the measured in situ stresses, as shown in Figure 2. Despite this overall trend, pronounced anomalies are observed for all three stress components in the upper-left corner of Figure 5. This area is close to the ground surface, where the in situ stress level would normally be expected to be relatively low; however, comparatively high stress values are obtained. This anomaly is mainly attributed to the valley-topography

effect in this region: during the MLR inversion, the y-direction displacement prescribed on the boundary at x = 529.6 can induce local stress concentration near the valley in the upper-left part of Figure 5. This concentration is then retained and/or amplified in the subsequent regression-based linear combination, leading to the anomalous stress zone. Faults also exert a significant influence on the in situ stress distribution in the study area, giving rise to zones of markedly reduced stress in and around the fault traces, which locally form belt-like low-stress regions (Figure 5b,c). Comparison with previous studies [11,18,19] suggests that the MLR inversion employed here tends to overestimate the spatial extent of the fault-affected stress perturbation zone. Overall, these features indicate that, although the MLR combined with the zone-stress loading method can reproduce the in situ stresses at the measurement points with reasonable accuracy, it may still introduce noticeable bias in the inversion and reconstruction of the in situ stress field.

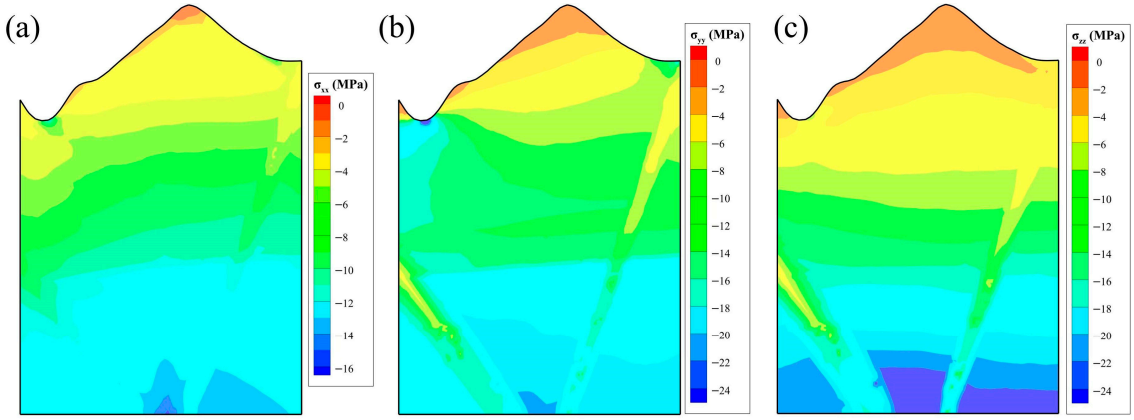


Figure 5. Contour plots of normal-stress components along the axis of the main powerhouse based on MLR inversion ((**a**) σ_{xx}; (**b**) σ_{yy}; (**c**) σ_{zz}).

To avoid potential differences in the inverted stress components caused by the choice of coordinate system, which may affect the analysis and comparison of the inverted in situ stress field, the contour plots of the three principal stresses along the powerhouse axial direction are further presented, as shown in Figure 6. The magnitudes of the principal stresses are invariant to coordinate-axis rotation and thus provide a frame-independent characterization of the stress state. Figure 6 indicates that the spatial distributions of three principal stresses are generally consistent with those of stress components in Figure 5, and both are influenced by burial depth and fault structures.

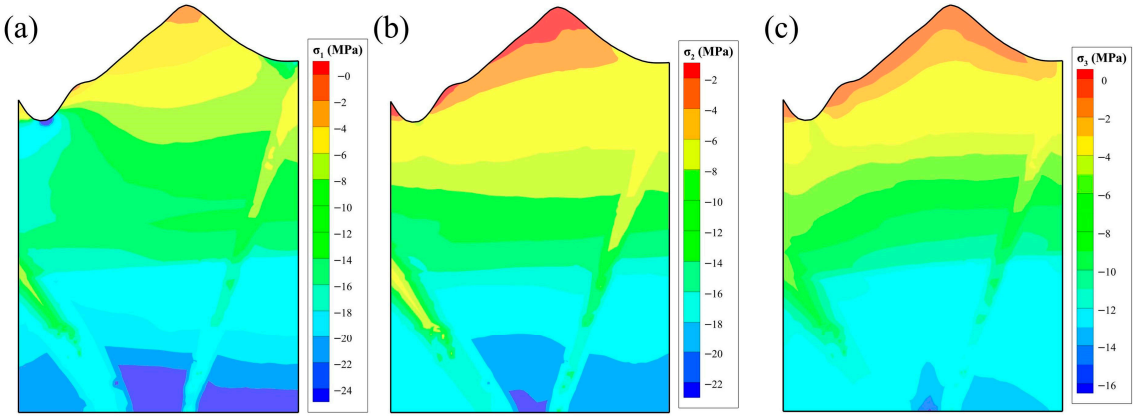


Figure 6. Contour plots of principal stresses along the axis of the main powerhouse based on MLR inversion ((**a**) σ_1; (**b**) σ_2; (**c**) σ_3).

4. In Situ Stress Inversion Using the PSO-SVR Algorithm

4.1. Basic Principles and Methods

For an undisturbed rock mass, the in situ stress field can be regarded as a superposition of two components: the self-weight (gravitational) stress and the tectonic stress. The self-weight stress is governed by the density of the rock and the local gravitational acceleration. Tectonic effects are mainly manifested as regional compression and shear; the compressive component can be represented by the lateral stress coefficients λ_x and λ_y in the x and y directions, respectively, whereas the shear component is described by the shear stresses τ_{xy}, τ_{yz}, and τ_{xz}. Within a given area, the gravitational acceleration and the density of the rock mass can be considered known. Accordingly, the in situ stress at any point in the rock mass can be expressed as a functional relationship of these parameters, as given in Equation (6) [20].

$$\sigma^g = f(\lambda_x, \lambda_y, \tau_{xy}, \tau_{yz}, \tau_{xz}) \tag{6}$$

SVR is an extension of the support vector machine framework to regression problems [21]. The basic idea is to map the input samples into a high-dimensional feature space through a nonlinear mapping and to construct an optimal hyperplane in that space, thereby achieving nonlinear regression in the original input space. For a training dataset $D = \{(x_i, y_i)\}^n_{i=1}$, the primal optimization problem can be converted into its dual form by introducing a kernel function, a loss function, and slack variables, and is then solved (e.g., by the Lagrange multiplier method or the sequential minimal optimization algorithm), yielding the following regression function:

$$f(x) = \sum_{i=1}^{n} (\alpha_i - \hat{\alpha}_i) k(x_i, x) + b \tag{7}$$

where α_i and $\hat{\sigma}_i$ are Lagrange multipliers, b is the bias term, and $k(x_i, x)$ is the kernel function.

In this study, a radial basis function (RBF) kernel is adopted. The RBF kernel implicitly maps the input data into a high-dimensional feature space via the kernel function, allowing a linear model in that space to represent highly nonlinear relationships in the original input space. It is therefore well suited to regression problems involving high dimensionality and pronounced nonlinearity.

To further enhance the prediction accuracy of the model, PSO is employed to perform a global search for the key SVR hyperparameters C and γ. In the PSO algorithm, each candidate solution is treated as a particle in a multidimensional parameter space, and particle positions and velocities are iteratively updated according to simple evolutionary rules so as to minimize the prediction error of the model. The mean squared error (MSE) is used as the objective function:

$$MSE = \frac{1}{n} \sum_{i=1}^{n} \left(\hat{b}^i - b^i \right)^2 \tag{8}$$

where $\hat{b}^i$ and b^i denote the inverted and measured values, respectively.

By coupling PSO with SVR, the resulting PSO-SVR algorithm combines the global optimization capability of PSO with the strong nonlinear regression capability of SVR, and can thus yield highly accurate and robust regression results for small-sample, high-dimensional, and nonlinear problems.

The procedure for in situ stress inversion using PSO-SVR is summarized as follows (see Figure 7):

Step 1: Ensure the ranges of the stress boundary-condition parameters λ_x, λ_y, τ_{xy}, τ_{yz}, and τ_{xz} and generate multiple combinations of boundary conditions using a uniform design scheme.

Step 2: For each boundary-condition combination, use the finite-difference code (FLAC3D 6.0) to compute the stress components at the measurement points.

Step 3: Assemble a dataset by taking the stress components at the measurement points as inputs and the corresponding stress boundary-condition parameters as outputs, and normalize the dataset.

Step 4: Specify the search ranges for the SVR hyperparameters C and γ, load the training samples, and apply PSO to iteratively optimize C and γ with respect to the MSE objective.

Step 5: Substitute the optimal values of C and γ into the SVR model to define the PSO-SVR model.

Step 6: Train the PSO-SVR model using the normalized training dataset to obtain the final optimal regression models.

Step 7: Input the measured in situ stress components into the trained PSO-SVR model(s) to predict the optimal stress boundary-condition parameters.

Step 8: Impose the optimal boundary conditions on the three-dimensional numerical model and perform forward finite-difference analysis to reconstruct the in situ stress field.

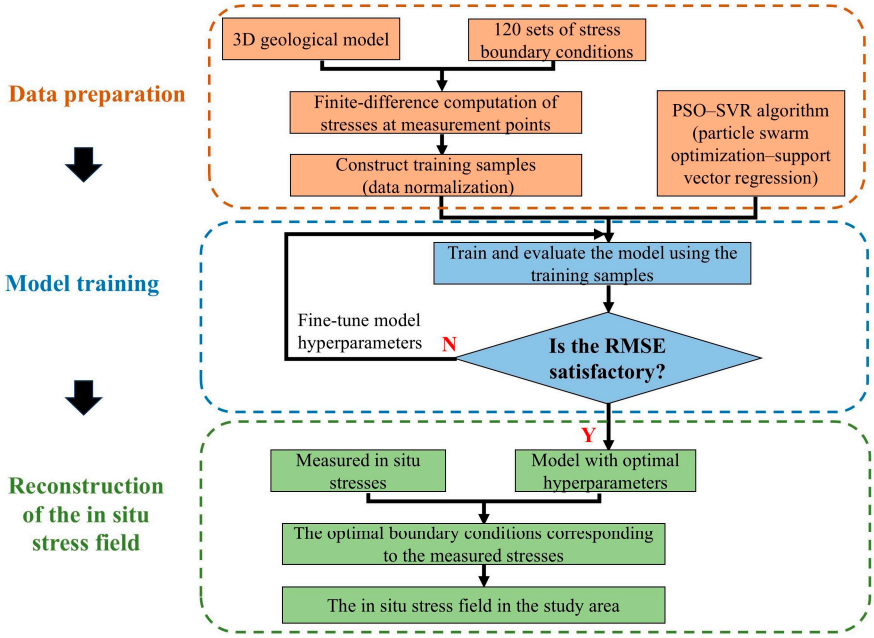


Figure 7. Flowchart of in situ stress inversion based on the PSO-SVR algorithm.

4.2. PSO-SVR Model Training and Prediction of Optimal Stress Boundary Conditions

The model mesh used for the PSO-SVR inversion is identical to that adopted in Section 3.2 (Figure 3) and all FLAC3D simulations employ the Mohr–Coulomb constitutive model and rock mass mechanical parameters as summarized in Table 2. Trial calculations under different combinations of stress boundary-condition parameters are carried out to determine the inversion variables, as listed in Table 5. A comparison between the measured and trial-calculated vertical stresses indicates noticeable discrepancies, which are attributed to uncertainties in the measurements and the geological parameters. After appropriate adjustment, a gravity acceleration of 10.9 m/s^2 is adopted in the subsequent analysis.

Table 5. Ranges of the stress boundary-condition parameters.

Inversion Parameter	λ_x	λ_y	τ_{xy} (MPa)	τ_{yz} (MPa)	τ_{xz} (MPa)
Range	0.50~1.25	0.81~1.50	−2.12~4.90	−2.22~1.03	−1.74~1.62

To ensure that the boundary conditions provide representative coverage of the parameter space, a $U_{120}(120^5)$ uniform design is adopted, in which 120 denotes the number of boundary-condition combinations and 5 is the number of factors (Table 6). These 120 sets of stress boundary conditions are applied to the three-dimensional mesh model, and stress components at the measurement points for each boundary-condition combination are computed using finite-difference analysis.

Table 6. Stress boundary conditions generated by the uniform design $U_{120}(120^5)$.

Number	λ_x	λ_y	τ_{xy} (MPa)	τ_{yz} (MPa)	τ_{xz} (MPa)
1	1.194	1.288	1.369	0.869	−0.432
2	0.510	0.867	0.540	−0.990	0.826
3	1.102	0.960	3.858	0.051	1.558
4	0.696	1.313	4.780	−1.692	1.414
5	1.069	1.023	−1.507	−1.459	1.149
6	1.040	0.813	3.217	0.666	−0.905
...	...	...	...	...	...
117	0.843	1.303	2.711	−0.146	−0.119
118	0.715	1.044	1.593	0.254	0.533
119	0.779	1.015	1.457	0.804	−0.466
120	0.988	1.098	0.657	−1.792	−1.063

Owing to differences in scale and noise among the five parameters of stress boundary-conditions, a dedicated PSO-SVR model is trained for each target (36 input features and one output) rather than a single multi-output model. This design reduces error coupling among outputs and allows target-specific hyperparameters (C, γ, ε), which is advantageous under limited-sample conditions. All models adopt an RBF kernel, and PSO is used to tune (C, γ, ε) so as to minimize the RMSE; the resulting optimal hyperparameters and corresponding RMSE values are summarized in Table 7. The stress components at the six measurement points are then fed into the trained PSO-SVR models to obtain the optimal combination of stress boundary-condition parameters, as listed in Table 8.

Table 7. PSO-SVR models with optimal parameters (RMSE: root mean squared error; C: penalty coefficient; γ: RBF kernel width; ε: insensitive zone).

Model	RMSE	C	γ	ε
Model_λ_x	0.001	1000.00	4.57×10^{-4}	0.003
Model_λ_y	0.011	1000.00	4.88×10^{-4}	0.006
Model_τ_{xy}	0.090	1000.00	2.95×10^{-4}	0.001
Model_τ_{yz}	0.075	1000.00	3.86×10^{-4}	0.026
Model_τ_{xz}	0.071	1000.00	4.28×10^{-4}	0.015

Table 8. The predicted optimal stress boundary conditions.

Inversion Parameters	λ_x	λ_y	τ_{xy} (MPa)	τ_{yz} (MPa)	τ_{xz} (MPa)
Value	0.606	1.467	2.891	0.765	−0.353

4.3. Inversion Results and Reconstructed In Situ Stress Field

By imposing the optimal stress boundary conditions given in Table 8 on the three-dimensional numerical model, the in situ stress field of the PSPS is reconstructed. The inverted stress components at the measurement points are compared with the measured values in Table 9. Overall, with the exception of σ_{xx} at measurement point YZK19(2) and σ_{yy} at measurement point YZK06(1), where the absolute deviations exceed 2 MPa, the

inverted normal stresses are generally in good agreement with the measured data. The MDR of the normal-stress components is 12.43%, and that of τ_{xy} is 64.81%, both lower than the corresponding values obtained from the MLR inversion. Nevertheless, in both inversion schemes the MDR of τ_{xy} remains significantly higher than that of the normal stresses, suggesting that the relatively large errors in τ_{xy} are more likely attributable to the inherent uncertainties and transformation assumptions in the hydraulic-fracturing measurements themselves than to the specific inversion methods.

Table 9. In situ stress results obtained by PSO-SVR algorithm (PS: predicted stress; MV: measured value).

ID	σ_{xx} (MPa)		σ_{yy} (MPa)		σ_{zz} (MPa)		τ_{xy} (MPa)		τ_{yz} (MPa)		τ_{xz} (MPa)	
	PS	MV	PS	MV	PS	MV	PS	MV	PS	MV	PS	MV
YZK06(1)	−2.3	−3.8	−2.5	−5.4	−4.4	−5.2	1.5	1.0	−0.4	0.0	0.0	0.0
YZK06(2)	−5.3	−6.1	−7.4	−8.7	−7.3	−8.2	1.3	1.7	−0.4	0.0	0.0	0.0
YZK17(1)	−10.0	−9.6	−12.7	−12.7	−12.0	−12.2	0.5	2.3	0.5	0.0	0.1	0.0
YZK17(2)	−11.2	−10.5	−15.3	−14.3	−14.1	−13.9	0.9	2.8	−0.2	0.0	−0.1	0.0
YZK19(1)	−11.0	−9.8	−15.7	−14.8	−12.9	−12.9	0.5	1.3	0.3	0.0	0.0	0.0
YZK19(2)	−12.0	−9.3	−14.9	−14.1	−13.6	−13.9	−0.1	1.3	0.0	0.0	0.0	0.0

The mesh density (or the number of elements) may affect the computed stresses at the measurement points. To verify the rationality of the mesh discretization adopted in this study, two additional reference models are established, and their numbers of zones and gridpoints are listed in Table 10. With the mechanical properties of the rock mass, the boundary conditions, and the parameters obtained from the PSO-SVR inversion kept identical, FLAC3D is used to compute the six stress components at the three measurement points for the three mesh models. The results are summarized in Table 11. As shown in Table 11, the differences in the same stress component at the same measurement point obtained from the three models with different mesh densities are small. The maximum deviation occurs for the σ_{zz} at YZK19(1), with a difference of 0.3 MPa, while the differences for all other stress components are within 0.2 MPa. These results indicate that the mesh discretization adopted in this study is reasonable and that the computed stresses are insensitive to mesh density.

Table 10. Numbers of zones and gridpoints for different FLAC3D models.

Model ID	Number of Gridpoints	Number of Zones
M-1	205,511	309,749
M-2 *	456,608	592,711
M-3	1,082,522	1,410,163

* Model M-2 is used in this paper.

Figure 8 presents contour plots of the three normal-stress components along the axis of the main powerhouse (x = 215 m) obtained from the PSO-SVR inversion. Overall, the stress field exhibits a relatively stable spatial pattern with few anomalous zones, and the relationship between stress and burial depth is clearer, with the three normal stresses generally increasing with depth. The contour maps also reflect the influence of topography on the in situ stress field: the σ_{zz} contours are broadly parallel to the ground-surface profile, and a local high-stress zone develops beneath the surface ridge. In addition, the fault still exerts a marked influence on the distribution of three stress components, producing pronounced fluctuations and reductions where the fault zone intersects the section. Figure 9 shows contour plots of the principal stresses, whose spatial patterns are broadly consistent with those of the corresponding normal-stress components in Figure 8.

The spatial distributions of the three principal stresses are jointly influenced by topographic variations and fault structures. In particular, σ_1 and σ_3 exhibit a more pronounced response to the fault, whereas σ_2 is more strongly controlled by topographic variations.

Table 11. Stress components at measurement points for different FLAC3D models.

Measurement Point	Model ID	σ_{xx} (MPa)	σ_{yy} (MPa)	σ_{zz} (MPa)	τ_{xy} (MPa)	τ_{yz} (MPa)	τ_{xz} (MPa)
YZK06(1)	M-1	−2.3	−2.6	−4.5	1.6	−0.3	−0.1
	M-2 *	−2.3	−2.5	−4.4	1.5	−0.4	0.0
	M-3	−2.3	−2.5	−4.3	1.5	−0.3	−0.2
YZK17(1)	M-1	−10.0	−12.7	−12.0	0.5	0.5	0.1
	M-2	−10.0	−12.7	−12.0	0.5	0.5	0.1
	M-3	−10.0	−12.5	−12.0	0.5	0.6	0.1
YZK19(1)	M-1	−11.0	−15.6	−12.8	0.5	0.2	0.0
	M-2	−11.0	−15.7	−12.9	0.5	0.3	0.0
	M-3	−11.2	−15.8	−13.1	0.5	0.3	0.0

* Model M-2 is used in this paper.

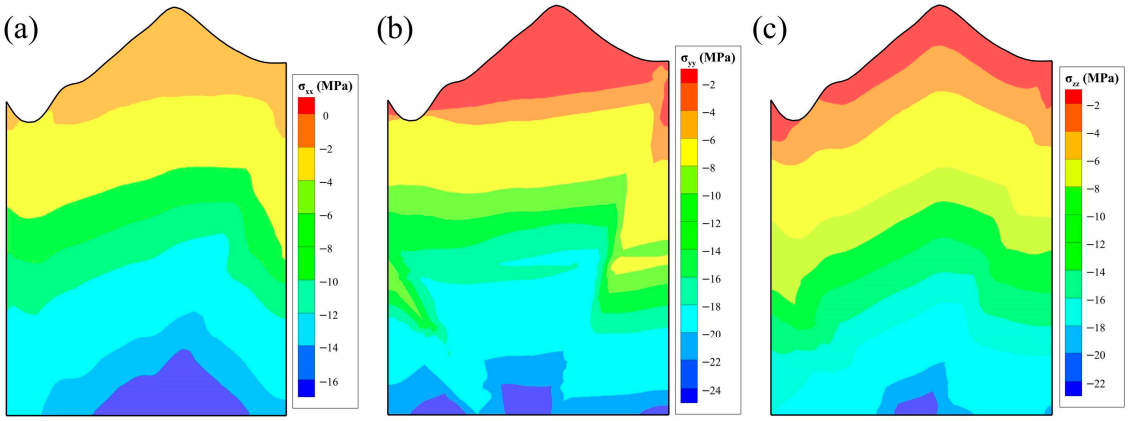


Figure 8. Contour plots of stress components along the axis of the main powerhouse based on the PSO-SVR algorithm ((**a**) σ_{xx}; (**b**) σ_{yy}; (**c**) σ_{zz}).

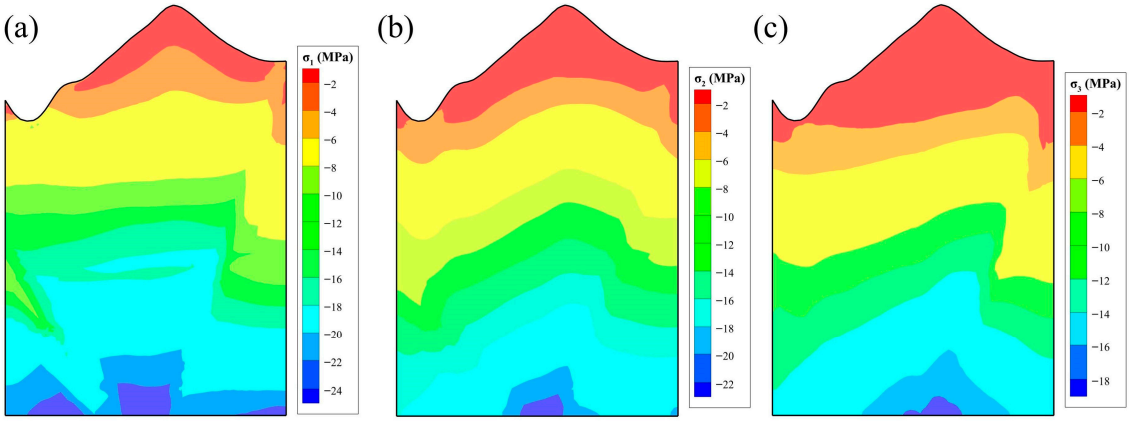


Figure 9. Contour plots of principal stresses along the axis of the main powerhouse based on the PSO-SVR algorithm ((**a**) σ_1; (**b**) σ_2; (**c**) σ_3).

Based on the inverted in situ stresses at the six measurement points in Table 8, the azimuths of the maximum principal stress with respect to the current coordinate system are calculated as 123.7°, 114.4°, 98.5°, 101.6°, 96.0°, and 88.0° (with the x direction defined as 0°, clockwise rotation, and the y direction as 90°). In the numerical coordinate system adopted in this study, the y-axis corresponds to the axis of the main powerhouse. Accordingly, the

acute angles between the maximum principal stress direction and the main powerhouse axis at the six points are 33.7°, 24.4°, 8.5°, 11.6°, 6.0°, and 2.0°, respectively. Excluding the first relatively large values, the angle between the maximum principal stress and the powerhouse axis in this area mainly falls within 2.0–24.4°. According to the general layout principle for underground caverns in PSPSs, the maximum principal stress should intersect the powerhouse axis at a small angle to reduce unfavorable deformation of the surrounding rock on the sidewalls. Based on this principle and the above angle range (2.0–24.4°), the selected orientation of the main powerhouse axis is considered reasonable.

The underground cavern group is located within X = 200–325 m, Y = 200–370 m, and Z = 280–345 m. The principal stress ranges reconstructed by the PSO-SVR inversion for this area are σ_1 = −14.74 to −19.05 MPa, σ_2 = −10.21 to −14.45 MPa, and σ_3 = −7.91 to −12.26 MPa. The caverns are mainly hosted in argillaceous siltstone and dolomite. Using an average saturated uniaxial compressive strength of 45 MPa, the ratio of rock strength to the maximum principal stress is 2.31–3.20, indicating a moderate in situ stress level in this area.

5. Discussion

Figure 10 compares the stress components obtained from the two inversion methods with the measured in situ stresses. Both methods reproduce σ_{xx} reasonably well, with predicted values close to the measurements at all points. For the other five stress components, however, the PSO-SVR results show smaller deviations from the measured values and smoother variations than those obtained by MLR. To provide a more quantitative comparison of the errors and the relative performance of the two methods, the root mean squared error (RMSE) and the mean absolute error (MAE) are used as evaluation metrics, defined as follows (Equations (9) and (10)):

$$\mathrm{RMSE} = \sqrt{\frac{1}{n}\sum_{i=1}^{n}(\hat{y}_i - y_i)^2} \tag{9}$$

$$\mathrm{MAE} = \frac{1}{n}\sum_{i=1}^{n}|\hat{y}_i - y_i| \tag{10}$$

where n is the number of samples, $\hat{y}_i$ is the inverted value, and y_i is the measured value.

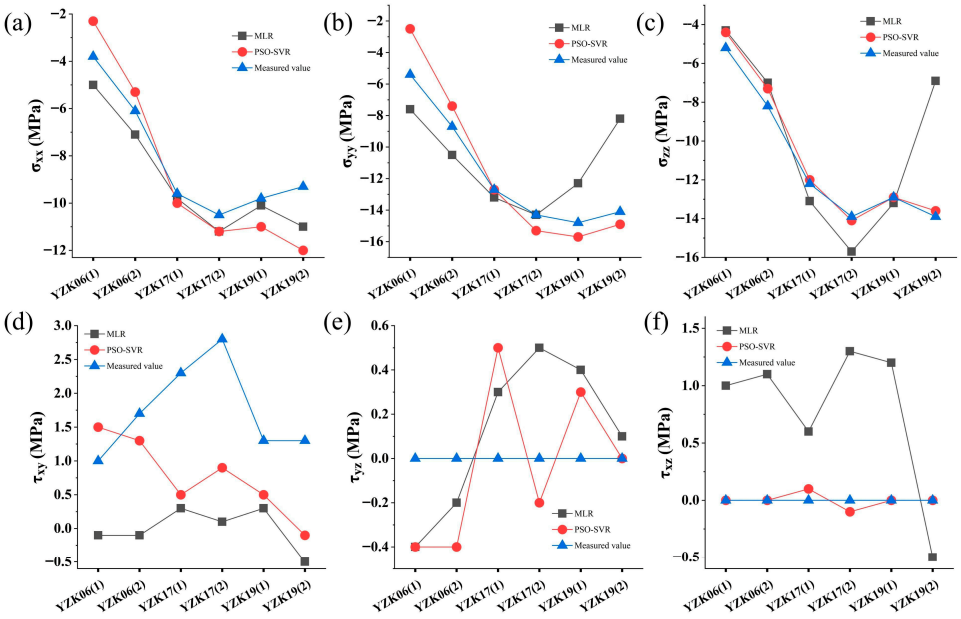


Figure 10. Comparison of stress components obtained by the two inversion methods with measured in situ stresses ((**a**) σ_{xx}; (**b**) σ_{yy}; (**c**) σ_{zz}; (**d**) τ_{xy}; (**e**) τ_{yz}; (**f**) τ_{xz}).

Figure 11 shows the overall RMSE and MAE values of the stress components obtained by the two inversion methods. For MLR, the RMSE and MAE are 1.95 and 1.34, respectively, whereas for PSO-SVR they are 1.01 and 0.71, corresponding to reductions of 48.21% and 47.01%. Since smaller RMSE and MAE values indicate better agreement with the measurements and higher predictive accuracy, these statistics demonstrate that the in situ stresses obtained using PSO-SVR are substantially closer to the measured values than those obtained using MLR.

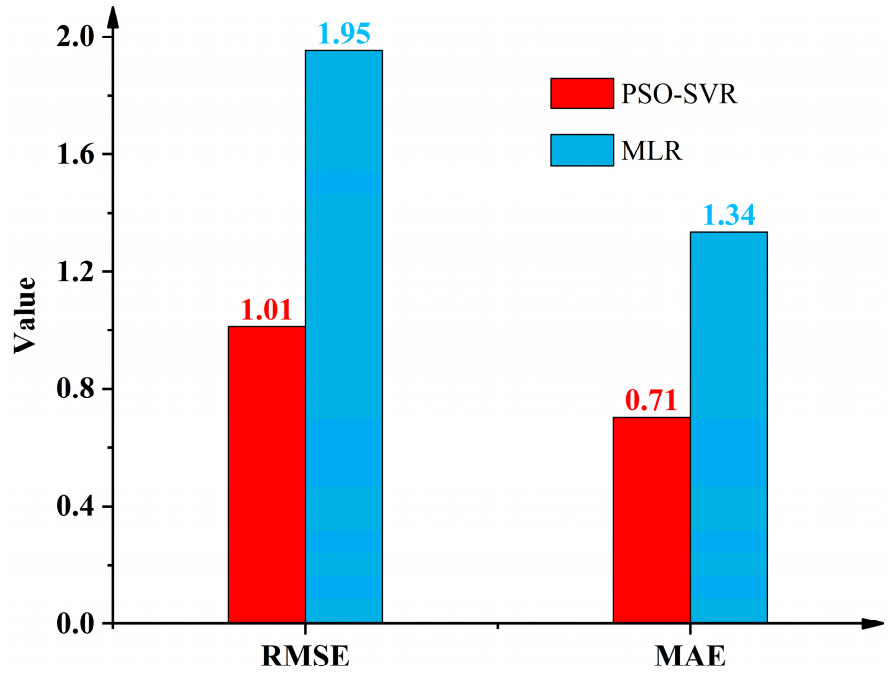


Figure 11. Statistical comparison of stress components obtained by the two inversion methods (RMSE: root mean squared error; MAE: mean absolute error).

Figure 12 presents the RMSE and MAE values for each of the six stress components. The two error indices exhibit broadly similar magnitudes and trends across the stress components. For σ_{xx}, the RMSE and MAE obtained by MLR are noticeably lower than those of PSO-SVR, indicating that MLR achieves higher inversion accuracy for this component. Meanwhile, for τ_{yz}, the statistical metrics of the two methods are close, suggesting comparable predictive performance. For the remaining four components, the RMSE and MAE obtained from PSO-SVR are consistently smaller than those from MLR, with particularly pronounced reductions for τ_{zz} and τ_{xz}, demonstrating that PSO-SVR provides a much more accurate prediction of these stress components.

A comparison of the stress contour plots obtained by the two methods (Figures 5, 6, 8 and 9) shows that the stress field reconstructed by the PSO-SVR inversion is more stable, exhibits a clearer relationship with burial depth, contains fewer anomalous stress zones, and reflects the influence of faults and topography on the stress distribution in a more geomechanically consistent manner. From a mechanistic point of view, the conventional MLR inversion inevitably relies on repeatedly applying different displacement or stress boundary conditions at the external model boundaries, both when computing the stress response under individual loading cases and when reconstructing the in situ stress field by superposing the elemental responses. This procedure tends to prolong the time required for the model to reach mechanical equilibrium and makes the solution particularly sensitive to boundary effects, so that artificial high- or low-stress zones may arise near model boundaries, in regions with strong mesh-size contrast, or in areas of complex topography and faulting. In other words, this "outside-in" strategy, in which external boundary conditions are continu-

ously adjusted to match internal stress measurements, has a clear physical interpretation. However, the coupling between boundary-condition updates and the equilibrium iterations can compromise the smoothness and spatial coherence of the reconstructed stress field. In contrast, the inversion approach based on lateral stress coefficients, PSO-driven hyperparameter search, and SVR model training can mitigate these shortcomings to some extent. By replacing traditional normal-stress or displacement boundary conditions at the outer boundaries with equivalent lateral pressure coefficients applied directly to the zones, while simultaneously constraining normal displacements on the model boundaries, the method keeps the boundary conditions more stable during the equilibrium process and reduces the spurious influence of boundary artifacts on the internal stress distribution. This interpretation is consistent with the observed improvements in smoothness and spatial coherence of the PSO-SVR stress field relative to the MLR.

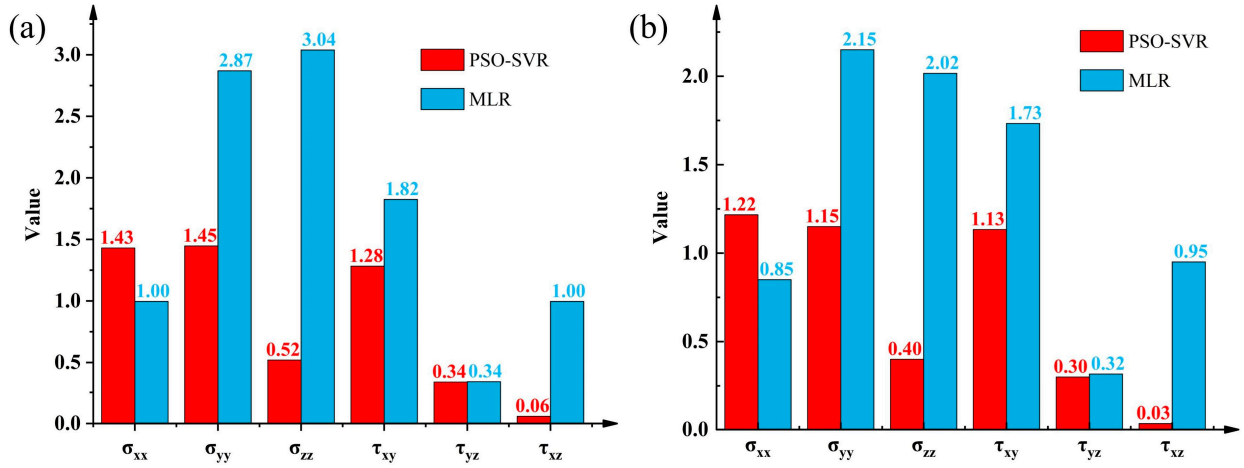


Figure 12. Statistical comparison of different stress components obtained by the two inversion methods ((**a**) RMSE; (**b**) MAE).

6. Conclusions

In this study, the engineering geological conditions and in situ stress characteristics of a PSPS are investigated, and a three-dimensional geological model with predominantly hexahedral elements is established. The in situ stress components at the measurement points and the stress field were inverted using both MLR and PSO-SVR. Comparison of the RMSE and MAE of the inverted stress components showed that the error indices associated with PSO-SVR are markedly smaller than those for MLR, indicating that the PSO-SVR inversion reproduces the measured stresses with higher accuracy. The main conclusions are as follows:

(1) The PSPS area is characterized by relatively simple layered Cambrian strata and a horizontal tectonic stress regime, with $\sigma_H > \sigma_v > \sigma_h$, a west–southwest-oriented maximum principal stress, and all three principal stresses increasing with burial depth.

(2) The MLR combined with the zone-stress loading method reproduces the in situ stresses at the measurement points ($R^2 = 0.894$), and the normal-stress components are generally consistent with the measured values. However, the reconstructed stress field contains numerous local stress anomalies and substantially exaggerates the influence of faults, so that noticeable discrepancies remain between the inverted and the actual in situ stress distribution.

(3) By defining the stress boundary conditions in terms of lateral stress coefficients and shear stresses and inverting them with a PSO-SVR algorithm, the stresses at the measurement points and the in situ stress field can be determined with good accuracy. Compared with

MLR combined with the zone-stress loading method, PSO-SVR yields lower RMSE and MAE values and a smoother stress field with fewer anomalous zones.

(4) From a mechanistic perspective, the PSO-SVR inversion based on lateral stress coefficients reduces artificial boundary effects compared with the conventional MLR scheme that repeatedly adjusts external displacement or stress boundaries, thereby yielding a smoother and more geomechanically consistent in situ stress field.

(5) The acute angle between the maximum principal stress and the main powerhouse axis mainly falls within 2.0–24.4°, indicating that the selected powerhouse axis orientation is reasonable. The reconstructed principal stress ranges in the underground cavern group are $\sigma_1 = -14.74$ to -19.05 MPa, $\sigma_2 = -10.21$ to -14.45 MPa, and $\sigma_3 = -7.91$ to -12.26 MPa, and the stress level is moderate (strength-to-maximum-stress ratio 2.31–3.20).

Author Contributions: Conceptualization, L.L., J.O. and Y.Z.; Methodology, L.L. and J.O.; Software, L.L. and G.N.; Validation, L.L.; Formal analysis, L.L., G.N. and N.L.; Investigation, L.L., J.O. and G.N.; Data curation, L.L. and G.N.; Writing—original draft, L.L. and J.O.; Writing—review and editing, L.L., J.O., G.N., Y.Z. and N.L.; Visualization, L.L. and J.O.; Supervision, J.O., Y.Z. and N.L.; Project administration, J.O. and Y.Z.; Funding acquisition, L.L., J.O. and Y.Z. All authors have read and agreed to the published version of the manuscript.

Funding: This research was funded by China Yangtze Power Co., Ltd., grant number 1524020050.

Institutional Review Board Statement: Not applicable.

Informed Consent Statement: Not applicable.

Data Availability Statement: The original contributions presented in this study are included in the article. Further inquiries can be directed to the corresponding authors.

Conflicts of Interest: Authors Liu, Jinhui Ouyang and Youping Zhu were employed by the company China Three Gorges Corporation. The remaining authors declare that the research was conducted in the absence of any commercial or financial relationships that could be construed as a potential conflict of interest. The authors declare that this study received funding from by China Yangtze Power Co., Ltd. The funder was not involved in the study design, collection, analysis, interpretation of data, the writing of this article or the decision to submit it for publication.

References

1. Meng, W.; He, C.; Zhou, Z.; Li, Y.; Chen, Z.; Wu, F.; Kou, H. Application of the Ridge Regression in the Back Analysis of a Virgin Stress Field. *Bull. Eng. Geol. Environ.* **2021**, *80*, 2215–2235. [CrossRef]
2. González de Vallejo, L.I.; Hijazo, T. A New Method of Estimating the Ratio between in Situ Rock Stresses and Tectonics Based on Empirical and Probabilistic Analyses. *Eng. Geol.* **2008**, *101*, 185–194. [CrossRef]
3. Gong, M.; Qi, S.; Liu, J. Engineering Geological Problems Related to High Geo-Stresses at the Jinping I Hydropower Station, Southwest China. *Bull. Eng. Geol. Environ.* **2010**, *69*, 373–380. [CrossRef]
4. Zhang, S.; Hu, A.; Wang, C. Three-Dimensional Inversion Analysis of an In Situ Stress Field Based on a Two-Stage Optimization Algorithm. *J. Zhejiang Univ.-Sci. A* **2016**, *17*, 782–802. [CrossRef]
5. Yan, H.-C.; Liu, H.-Z.; Li, Y.; Zhuo, L.; Xiao, M.-L.; Chen, K.-P.; Wu, J.-M.; Pei, J.-L. Inversion Analysis of the In Situ Stress Field around Underground Caverns Based on Particle Swarm Optimization Optimized Back Propagation Neural Network. *Appl. Sci.* **2023**, *13*, 4697. [CrossRef]
6. Guo, M.; Yin, S.; Li, C.; Wang, S. 3D In Situ Stress Estimation by Inverse Analysis of Tectonic Strains. *Appl. Sci.* **2021**, *11*, 5284. [CrossRef]
7. Luo, M.-R.; Zhang, C.-Y.; Wang, B.; Zeng, Y.-H. Discrete Element-Based Regression Analysis of Initial Ground Stress and Application to an Extra-Long Tunnel in China. *Bull. Eng. Geol. Environ.* **2023**, *82*, 405. [CrossRef]
8. Meng, W.; Zhou, H.; Luo, C.; Qin, S.; Zhang, X.; Chen, B. Multiple Linear Regression Inversion of the Ground Stress Field in Rock Masses for Tunnel Engineering: A Novel Approach to Stress Field Reconstruction. *Buildings* **2025**, *15*, 547. [CrossRef]
9. Li, Y.; Guo, Y.; Zhu, W.; Li, S.; Zhou, H. A Modified Initial In-Situ Stress Inversion Method Based on FLAC3D with an Engineering Application. *Open Geosci.* **2015**, *7*, 20150065. [CrossRef]

10. Chen, B.; Ren, Q.; Wang, F.; Zhao, Y.; Liu, C. Inversion Analysis of In-Situ Stress Field in Tunnel Fault Zone Considering High Geothermal. *Geotech. Geol. Eng.* **2021**, *39*, 5007–5019. [CrossRef]
11. Zhou, Z.; Chen, Z.; Wang, B.; Jiang, C.; Li, T.; Meng, W. Study on the Applicability of Various In-Situ Stress Inversion Methods and Their Application on Sinistral Strike-Slip Faults. *Rock Mech. Rock Eng.* **2023**, *56*, 3093–3113. [CrossRef]
12. Li, G.; Hu, Y.; Li, Q.-B.; Yin, T.; Miao, J.-X.; Yao, M. Inversion Method of In-Situ Stress and Rock Damage Characteristics in Dam Site Using Neural Network and Numerical Simulation—A Case Study. *IEEE Access* **2020**, *8*, 46701–46712. [CrossRef]
13. Song, Z.; Jiang, Q.; Chen, P.; Xia, Y.; Xiang, T. Nonlinear Intelligent Inversion Method and Practice for In-Situ Stress in Stratified Rock Masses with Deep Valley. *Rock Mech. Rock Eng.* **2025**, *58*, 1933–1955. [CrossRef]
14. Li, Q. Research on Geostress Inversion Method of Computer Big Data Technology in Support Vector Regression Algorithm. In Proceedings of the 2022 IEEE 2nd International Conference on Power, Electronics and Computer Applications (ICPECA), Shenyang, China, 21–23 January 2022; pp. 810–814.
15. Bao, T.; Cheng, J.; Xing, Y.; Zhou, X.; Chen, Y.; Zhao, X. Inversion of Initial In-situ Stress Field of Underground Caverns of Hydropower Station Based on GD-PSO. *J. Zhengzhou Univ. (Eng. Sci.)* **2025**, *46*, 130. [CrossRef]
16. Zhang, P. In Situ Stress Inversion and Distribution Characteristics of Tunnel Based on Numerical Simulation and Neural Network Technology. *Shock Vib.* **2021**, *2021*, 5545283. [CrossRef]
17. Zhou, Z.; Chen, H.; Luo, T.; Fu, S. A simple inversion method for initial ground stress of underground powerhouses based on FLAC3D. *Eng. J. Wuhan Univ.* **2024**, *57*, 11–15.
18. Li, T.; Chen, Z.; Zhou, Z.; Bao, Y. In Situ Stress Distribution Law of Fault Zone in Tunnel Site Area Based on the Inversion Method with Optimized Fitting Conditions. *Front. Earth Sci.* **2023**, *10*, 1031985. [CrossRef]
19. Fu, H.; Li, J.; Li, G.; Chen, J.; An, P. Determination of In Situ Stress by Inversion in a Superlong Tunnel Site Based on the Variation Law of Stress—A Case Study. *KSCE J. Civ. Eng.* **2023**, *27*, 2637–2653. [CrossRef]
20. Liu, Q.; Wang, D.; Zhu, Y.; Yang, Z.; Bo, Y. Application of support vector regression algorithm in inversion of geostress field. *Rock Soil Mech.* **2020**, *41*, 319–328. [CrossRef]
21. Smola, A.J.; Schölkopf, B. A Tutorial on Support Vector Regression. *Stat. Comput.* **2004**, *14*, 199–222. [CrossRef]

Disclaimer/Publisher's Note: The statements, opinions and data contained in all publications are solely those of the individual author(s) and contributor(s) and not of MDPI and/or the editor(s). MDPI and/or the editor(s) disclaim responsibility for any injury to people or property resulting from any ideas, methods, instructions or products referred to in the content.